




On Mapping Exoplanet Atmospheres with High-dispersion Spectro-polarimetry: Some Model Predictions

A. García Muñoz 

Zentrum für Astronomie und Astrophysik, Technische Universität Berlin, Hardenbergstrasse 36, D-10623 Berlin, Germany
garciamunoz@astro.physik.tu-berlin.de, tonhingg@gmail.com

Received 2017 November 30; revised 2018 January 10; accepted 2018 January 21; published 2018 February 16

Abstract

Planets reflect and linearly polarize the radiation that they receive from their host stars. The emergent polarization is sensitive to aspects of the planet’s atmosphere such as the gas composition and the occurrence of condensates and their optical properties. Extracting this information will represent a major step in the characterization of exoplanets. The numerical simulations presented here show that the polarization of a spatially unresolved exoplanet may be detected by cross-correlating high-dispersion linear polarization and intensity (brightness) spectra of the planet–star system. The Doppler shift of the planet-reflected starlight facilitates the separation of this signal from the polarization introduced by the interstellar medium and the terrestrial atmosphere. The selection of the orbital phases and wavelengths at which to study the planet is critical. An optimal choice, however, will partly depend on information about the atmosphere that is a priori unknown. We elaborate on the cases of close-in giant exoplanets with non-uniform cloud coverage, an outcome of recent surveys of brightness phase curves from space, and for which the hemispheres east and west of the substellar point will produce different polarizations. With integration times of the order of hours at a 10 m telescope, the technique might distinguish among some proposed asymmetric cloud scenarios with fractional polarizations of 10 parts per million for one such planet orbiting a $V\text{-mag} = 5.5$ host star. Future 30–40 m telescopes equipped with high-dispersion spectro-polarimeters will be able to investigate the linear polarization of smaller planets orbiting fainter stars and look for molecular features in their polarization spectra.

Key words: planets and satellites: atmospheres – planets and satellites: gaseous planets – polarization – radiative transfer – techniques: polarimetric

1. Introduction

Whole-disk polarization measurements of reflected sunlight have a long history in the remote sensing of the bodies of the solar system, their surfaces and atmospheres (e.g., Mishchenko et al. 2010; Kolokolova et al. 2015). Linear polarimetry (the focus of this work) is potentially more sensitive than brightness measurements to the composition, size, and shape of the scattering particles. The two approaches complement each other in the characterization of the condensate–gas envelope of an atmosphere (Hansen & Travis 1974). Venus and Titan are classical examples of how polarization has contributed to our understanding of atmospheres. The polarization of Venus varies strongly with wavelength and phase angle, and shows specific features (glory, primary rainbow) that can only be ascribed to spherical (and thus liquid) droplets of a narrow size distribution and refractive index consistent with sulfuric acid in water (Hansen & Hovenier 1974). Titan strongly polarizes the incident sunlight, with fractional polarizations of up to 40%–70% at quadrature for wavelengths from the ultraviolet to the near-infrared (Tomasko & Smith 1982; West et al. 1983). This Rayleigh-like behavior in polarization, combined with evidence for non-Rayleigh-like strong forward scattering in intensity, is at the core of the interpretation of Titan’s ubiquitous haze as forming by aggregation of thousands of nanometer-size monomers produced through photochemical processes (West & Smith 1991; Lavvas et al. 2013).

The potential and current status of polarimetry for the detection of exoplanets and the characterization of their atmospheres and orbits has been discussed at length (e.g., Seager et al. 2000; Stam et al. 2004; Fluri & Berdyugina 2010;

Fossati et al. 2012; Wiktorowicz & Stam 2015). Since polarimetry is a photon-starved technique, most efforts (e.g., Berdyugina et al. 2008; Lucas et al. 2009; Wiktorowicz et al. 2015; Bott et al. 2016) have focused on broadband polarization from bright star systems (55 Cancri, τ Boötes, HD 189733). To date, the only claim for exoplanet polarization refers to HD 189733 b, a hot Jupiter orbiting a $V\text{-mag} = 7.7$, K-type active star (Berdyugina et al. 2008, 2011), but the detection remains contested (Wiktorowicz et al. 2015; Bott et al. 2016). Exoplanet polarization will eventually transition into an undisputed reality, and that step will open unprecedented possibilities for the characterization of their atmospheres.

Broadband polarimetry ensures that a large number of photons are collected, which is essential for reaching the required sensitivities of tens of parts per million (ppm) or better. On the other hand, broadband polarimetry also requires the removal of systematics introduced by the telescope–instrument optical system, and the subtraction of the polarization arising in the interaction of the starlight with the interstellar medium (ISM) or with the terrestrial atmosphere. In reality, the non-planet components of the measured polarization signal can easily bury the polarization caused by the planet. These technical challenges are driving fast progress in polarimetry at the ppm level, including the definition of standard stars and the understanding of instrumental polarization, and in the polarimetric charting of the ISM (e.g., Fossati et al. 2007; Lucas et al. 2009; Wiktorowicz 2009; Bailey et al. 2015; Cotton et al. 2016, 2017; Cikota et al. 2017). Ultimately, achieving sensitivities at the ppm level will require the joint optimization of each of these aspects.

An alternative to broadband polarimetry is the use of high-dispersion spectro-polarimetry together with some form of cross-correlation (HDSP-CC hereafter). The idea was first presented by Moutou et al. (2007), but not developed in depth. The authors failed to find the polarized signal of HD 189733 b in measurements carried out with the ESPaDOnS instrument at the 3.6 m Canada–France–Hawaii telescope, probably because the signal-to-noise ratio (S/N) of their measurements was insufficient. In recent years, the HDS-CC technique (without polarimetry) has become established as a powerful tool in the compositional and dynamical investigation of exoplanet atmospheres (e.g., Snellen et al. 2010, 2014; Rodler et al. 2012; Lovis et al. 2017). The technique benefits from the spectral separation of the planet and the star due to their relative Doppler shifts and from the use of a priori information about the atmospheric feature being searched for in the form of a template spectrum. After a few unfruitful attempts (e.g., Charbonneau et al. 1998; Collier Cameron et al. 1999; Rodler et al. 2013), Martins et al. (2015) recently reported the detection of reflected starlight from the non-transiting hot Jupiter 51 Peg b. The authors inferred a geometric albedo $A_g = 0.5 \times (1.9/(R_p/R_J))^2$, which is degenerate with the undetermined planet radius (in Jovian units) R_p/R_J . This is a large albedo for any R_p/R_J consistent with models of planet structure, and makes the planet stand out among more typical values of $A_g < 0.2$ for hot Jupiters (Angerhausen et al. 2015; Esteves et al. 2015). Regardless of the precise value for 51 Peg b’s geometric albedo, the detection represents a milestone for the consolidation of the HDS-CC technique in investigations of reflected starlight.

The present work elaborates on the HDSP-CC technique in its application to the characterization of exoplanet atmospheres. Making its case is timely because there are a number of spectro-polarimeters (e.g., ESPaDOnS, PEPSI, HARPSpol, SPIRou) (Donati et al. 2006; Snik et al. 2008; Artigau et al. 2014; Strassmeier et al. 2015) either available or being commissioned at 4–10 m telescopes, and instrument concepts under consideration for next-generation space telescopes such as LUVOIR/POLLUX.¹ The paper is split as follows. In Section 2, we introduce the scientific case selected to demonstrate some practical aspects of the technique. Section 3 presents our fiducial planet and the idealized photometric model that enables us to explore the performance of the technique, and Section 4 discusses the outcome of the numerical simulations. Finally, in Section 5 we summarize the main conclusions and anticipate future avenues to explore.

2. Patchy Clouds on Hot Jupiters

Observations with the *Kepler* mission (photometric precisions of a few ppm over multi-year baselines, sensitive to 0.4–0.9 μm radiation of effective wavelength $\lambda_{\text{eff}} \approx 0.65 \mu\text{m}$) have enabled the atmospheric investigation of ~ 20 transiting exoplanets over their full orbit (e.g., Shporer 2017 for a review). A conclusion drawn from such studies is that the whole-disk brightness of close-in giant planets (hot Jupiters) may peak before, at, or after occultation (Demory et al. 2013; Angerhausen et al. 2015; Esteves et al. 2015). This lack of symmetry in the brightness phase curves is explained through an asymmetry in the planets’ envelopes. For the hotter (cooler) planets, the brightness tends to peak before (after) occultation

(Esteves et al. 2015). Simulations with General Circulation Models (GCMs) provide valuable context for understanding this trend on the basis of how the energy is transported on the global scale. The atmospheric super-rotation generally predicted by GCMs will shift the planet’s hot spot eastwards from the substellar point.² At high temperatures, thermal emission from the hot spot would dominate the planet’s signal, thereby introducing a pre-occultation brightness peak. In contrast, cooler equilibrium temperatures would facilitate the formation of clouds on the night side, which are transported by the eastwards jets onto the dayside, where they ultimately evaporate (Showman et al. 2008; Oreshenko et al. 2016; Parmentier et al. 2016; Roman & Rauscher 2017). For these planets, the resulting non-uniform cloud distribution would boost the planet’s reflectivity after occultation.

Among the planets with post-occultation peaks, Kepler-7b has received significant attention (Demory et al. 2013; García Muñoz & Isaak 2015; Hu et al. 2015; Oreshenko et al. 2016; Parmentier et al. 2016; Roman & Rauscher 2017) and become a reference for what will be possible in the near future with the phase curves to be delivered by missions such as *CHEOPS* (Fortier et al. 2014), *JWST*, *TESS* (Ricker et al. 2015), or *PLATO* (Rauer et al. 2014) targeting brighter stars. For this reason, we will hereafter use the atmospheric structure inferred for this planet to demonstrate the HDSP-CC technique. This choice serves also to highlight the synergies between multi-facility investigations.

Kepler-7b is a giant ($R_p/R_J = 1.61$), low-density ($\rho_p/\rho_J = 0.14$) exoplanet orbiting a G-type star (Latham et al. 2010) and exhibits an unusually high geometric albedo for a hot Jupiter of ~ 0.30 (Demory et al. 2013; García Muñoz & Isaak 2015). The non-detection of occultations at 3.6 and 4.5 μm with *Spitzer* confirms that the brightness over the *Kepler* passband is dominated by reflected starlight rather than by thermal emission (Demory et al. 2013). In the currently accepted scenario, the post-occultation peak in Kepler-7b’s phase curve is caused by clouds displaced toward the dawn terminator that break the east–west symmetry, boost the reflectance, and locally mask the absorbing gas below the cloud.

García Muñoz & Isaak (2015) proposed a scenario that synthesizes the above ideas while allowing the investigation of cloud properties such as the optical thickness, horizontal extent, and displacement from the substellar point, the optical properties of the condensates, and the overall reflectance of the gas below the cloud. By solving the multiple-scattering radiative transfer problem for millions of configurations, each exploring a combination of the model properties, and the χ^2 comparison of the synthetic phase curves to the measurements, the authors identified the continuum of cloud–gas configurations that best reproduce the brightness phase curve of Kepler-7b. This continuum is generally characterized by a thick cloud displaced toward the dawn terminator and resting above strongly absorbing gas. The cloud consists of particles that scatter the incident starlight with a single scattering albedo close to one, thereby imparting to the planet its overall large reflectance. The equilibrium temperature of the planet, $T_{\text{eq}} \sim 1630 \text{ K}$ (García Muñoz & Isaak 2015), sets another constraint because at temperatures loosely related to T_{eq} only a few plausible

¹ <https://asd.gsfc.nasa.gov/luvoir/>

² We adopt the convention that close-in giant exoplanets are tidally locked and follow prograde orbits. Hence the equivalence between west and dawn, and east and dusk.

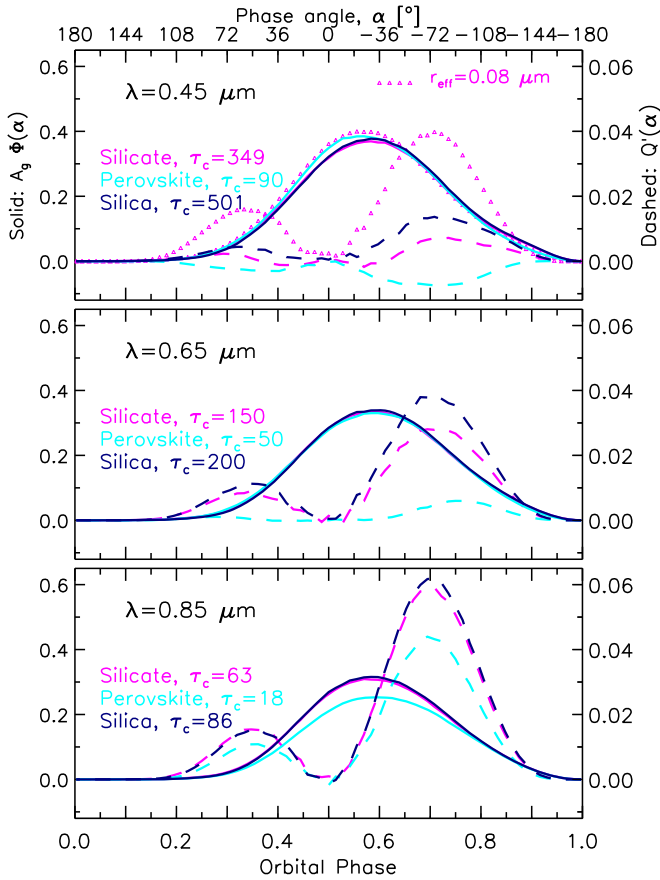


Figure 1. Synthetic phase curves of brightness and polarization based on the best fits by García Muñoz & Isaak (2015) to the brightness measurements of Kepler-7b ($\lambda_{\text{eff}} = 0.65 \mu\text{m}$) (Demory et al. 2013). Three condensate compositions plausibly explain the measurements, namely silicate, perovskite, and silica. Referring to the model in García Muñoz & Isaak (2015) with a Mie treatment of the cloud particles, each cloud–gas configuration is described by five parameters: τ_c , σ_c , $-\Delta\phi_c$, r_{eff} , and r_g . Our calculations here adopt $r_g = 0$ for all three condensates. Additionally, for silicate: $\sigma_c = 30^\circ$, $-\Delta\phi_c = 80^\circ$, $r_{\text{eff}} = 0.13 \mu\text{m}$; for perovskite: $\sigma_c = 25^\circ$, $-\Delta\phi_c = 55^\circ$, $r_{\text{eff}} = 0.1 \mu\text{m}$; for silica: $\sigma_c = 30^\circ$, $-\Delta\phi_c = 85^\circ$, $r_{\text{eff}} = 0.13 \mu\text{m}$. The optical thickness at the cloud center, τ_c , for each condensate and wavelength is quoted in the corresponding graph. τ_c over the *Kepler* passband ($\lambda_{\text{eff}} = 0.65 \mu\text{m}$) was obtained from the fit to the measurements; at the other wavelengths, τ_c is estimated on the basis of the ratio of particle extinction cross sections at the corresponding wavelength and at $0.65 \mu\text{m}$.

condensate compositions are consistent with nearly conservative scattering. In the framework of Mie theory (strictly valid only for spherical particles) the authors further constrain the refractive index and particle size of the cloud particles. The inferred effective radii are: $0.1\text{--}0.32 \mu\text{m}$ for silicate (refractive index, $n \approx 1.6 + i10^{-4}$); $0.08\text{--}0.2 \mu\text{m}$ for perovskite ($n \approx 2.25 + i10^{-4}$); $0.1\text{--}0.4 \mu\text{m}$ for silica ($n \approx 1.5 + i10^{-7}$). The quoted intervals bracket four standard deviations relative to the optimal solutions for each condensate. The proposed scenarios are consistent with the expectation that the gas phase of hot-Jupiter atmospheres over the *Kepler* passband is strongly absorbing due to the occurrence of alkalis at the altitudes being probed by reflected starlight photons (Seager et al. 2000; Sudarsky et al. 2000). For Kepler-7b, the hypothesized cloud, if at high altitude, would mute the alkali absorption, especially after occultation. Kepler-7b’s low gravity, which helps small particles to stay suspended high in the atmosphere, may be key to explaining its elevated albedo (Sudarsky et al. 2000).

Figure 1(middle) shows (solid lines) the synthetic phase curves for the cloud–gas configurations that best reproduce the Kepler-7b measurements, as inferred by García Muñoz & Isaak (2015) (see caption for additional details). They are characterized by $r_{\text{eff}} = 0.13 \mu\text{m}$ for silicate and silica, and $0.1 \mu\text{m}$ for perovskite. The corresponding polarization phase curves are also shown (dashed lines). All simulations were done with a backward Monte Carlo algorithm (García Muñoz & Mills 2015) as described in García Muñoz & Isaak (2015). The scattering matrices for each condensate were obtained with the Mie theory model of Mishchenko et al. (2002). By construction, the three cloud–gas configurations produce brightness phase curves that are indistinguishable over the *Kepler* passband. In contrast, the dashed curves of Figure 1(middle) show that each cloud–gas configuration will linearly polarize the incident starlight differently. We represent the Stokes vector for the irradiance from the planet, normalized to the irradiance of the (essentially) unpolarized star, as $(R_p/a)^2[A_g\Phi, Q', U', V']$. The term Q' used in the representation of Figure 1 is sometimes called polarized intensity (Buenzli & Schmid 2009) and is the linear polarization equivalent of the size-normalized representation for the planet’s brightness $A_g\Phi$. U' is the linearly polarized intensity at 45° rotation and V' is the circularly polarized intensity. A_g and $\Phi(\alpha)$ stand for the geometric albedo and the planet’s phase law, respectively, and by convention $\Phi(\alpha = 0) \equiv 1$. Each of the elements in brackets for the planet’s Stokes vector depends on both α and λ . We occasionally omit one of these dependences to highlight the other. Neglecting U' and V' , the fractional polarization of the stand-alone planet, i.e., if spatially resolved from its host star, is given by the ratio $Q'/A_g\Phi$.

In Mie theory, the scattering matrix that goes into the radiative transfer equation is sensitive to the refractive index (and in turn the composition) and the size parameter ($x_{\text{eff}} = 2\pi r_{\text{eff}}/\lambda_{\text{eff}}$) of the scatterers. If the particles are not spherical, then Mie theory does not apply and the particles’ shape becomes an extra factor to consider (Mishchenko et al. 2010). As in García Muñoz & Isaak (2015), we will here assume sphericity of the scattering particles as a convenient approach to connect the microscopic characteristics of the cloud particles, their optical properties, and the overall appearance of the planet. This pragmatic simplification might eventually be tested with polarization data since Mie theory results in well-defined predictions.

The simulations of Q' in Figure 1(middle) reveal the power of polarization to discriminate between cloud–gas configurations that produce no distinguishable behavior in brightness. The asymmetry in the brightness phase curves is mirrored by two distinct peaks in the pre-occultation (orbital phase, $\text{OP} < 0.5$; $\alpha > 0$) and post-occultation ($\text{OP} > 0.5$; $\alpha < 0$) polarizations. Both $A_g\Phi$ and Q' peak at $\text{OP} > 0.5$. The ratio $Q'/A_g\Phi$ (not shown here) peaks nearer to quadrature ($|\alpha| \sim 90^\circ$) and is larger for $\text{OP} \sim 0.25$ than for $\text{OP} \sim 0.75$. Detecting the pre- and post-occultation polarization will help confirm or rule out some of the proposed asymmetric cloud–gas scenarios, thereby helping map the planet.

We have predicted the planet’s phase curves at other wavelengths. To that end, we recalculated the cloud’s optical thickness (which is proportional to the particles’ extinction cross section), and the scattering matrix and single scattering albedo of the particles. Figures 1(top) and (bottom) present the phase curves at $\lambda_{\text{eff}} = 0.45$ and $0.85 \mu\text{m}$. Again, minor differences in

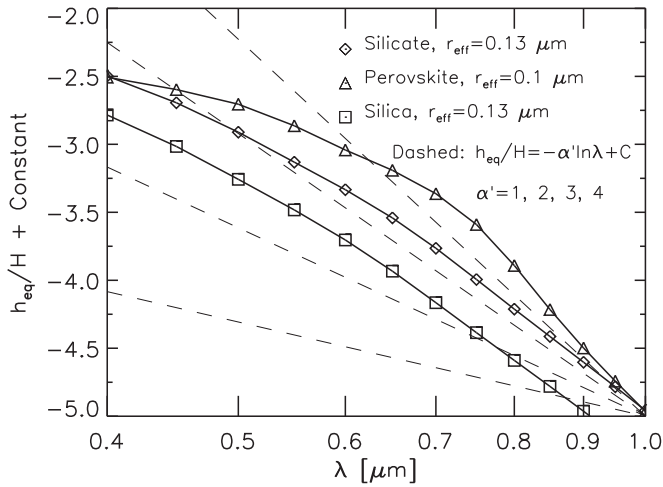


Figure 2. Variation with wavelength of the atmospheric equivalent height normalized to the scale height. To within a good approximation, h_{eq}/H depends linearly on $\ln \sigma(\lambda)$, where σ is the extinction cross section of the scattering particles that interact with the starlight at the optical radius level (i.e., the level at which the limb optical thickness is approximately 0.56; Lecavelier des Etangs et al. 2008). The solid curves represent h_{eq}/H for the properties of the cloud particles described in Figure 1. The dashed curves are further simplified representations of h_{eq}/H that assume $\sigma \propto \lambda^{-\alpha'}$.

brightness can correspond to major differences in polarization. From top to bottom, the polarization phase curves in Figure 1 evolve into a Rayleigh-like behavior, i.e., increasingly positive $Q'/A_g \Phi$ ratios near quadrature (Buenzli & Schmid 2009), as the size parameter x_{eff} decreases.

The simulations of Figure 1 are based on one-slab representations of the atmosphere that do not distinguish between multiple vertical layers. In particular, the simulations do not include a separate gas or haze layer on top of the column-averaged cloud. In brightness measurements over the *Kepler* passband, the contribution from such a layer is either embedded in the cloud properties inferred by García Muñoz & Isaak (2015) or is small in the near-nadir view at which the brightness phase curve is more constraining. Indeed, a planet-wide, optically thick Rayleigh-scattering layer on top of the cloud would produce no post-occultation peak in *Kepler*-7b’s brightness phase curve. Such a gas/haze layer might negligibly affect the brightness phase curve (depending on its optical thickness) while substantially modifying the polarizing properties of the atmosphere (which is dictated by the optical depths ≤ 1 as measured from the top of the atmosphere) (Buenzli & Schmid 2009). The triangle phase curves in Figure 1(top) illustrate this point. They were produced with the same combination of model parameters as for the silicate simulations, except that a smaller particle size $r_{eff} \approx 0.08 \mu\text{m}$ was implemented. Although the overall planet brightness is not significantly affected, a decreased x_{eff} results in an increased Rayleigh-like polarization. The above examples show that asymmetries in the planet’s phase curve can correspond to asymmetric polarizations, and that Q' can take a range of values that are poorly constrained by the brightness measurements. In turn, measuring Q' would help distinguish between some of the proposed scenarios.

If the planet was viewed in transmission, the small particles ($r_{eff} = 0.1\text{--}0.13 \mu\text{m}$) used for the simulations in Figure 1 would produce a Rayleigh slope at short wavelengths. This is seen in Figure 2, which shows the equivalent height of the

atmosphere normalized to the pressure scale height for wavelengths from 0.4 to $1 \mu\text{m}$ according to the analytical treatment of Lecavelier des Etangs et al. (2008). Thus, atmospheres with Rayleigh slopes in transmission or with moderately large geometric albedos do not necessarily produce Rayleigh-like polarization phase curves across the UV–NIR spectrum.

The sensitivity of polarization to wavelength is a two-edged sword. Multi-wavelength polarization measurements probing a range of x_{eff} values will likely experience a broader range of behaviors than the corresponding brightness. This sensitivity will translate into stronger constraints on the atmosphere. On the other hand, measurements averaging over a broad spectral range may inadvertently wash out the wavelength-dependent response of the atmosphere and result in an erroneous interpretation. Similarly, because Q' depends on α in a less predictable way than $A_g \Phi$, measurements over a broad range of phase angles may partly wash out the information encoded in the polarization phase curves. These arguments have implications for the design of prospective observations. Ideally, one would carry out the polarization observations at a range of phase angles that maximize the planet polarization, and at wavelengths that optimize the responses of both planet and star to the HDSP-CC technique. The latter is discussed below.

3. Photometric Model

The fiducial planet–star system that serves us to explore the HDSP-CC technique is constructed by combining the orbital properties and star magnitude of the 51 Peg system and the atmospheric properties inferred for *Kepler*-7b. In other words, we consider in our exercise that 51 Peg b’s atmosphere is similar to the atmosphere of *Kepler*-7b. The assumption is speculative but not necessarily far-fetched because both planets have similar equilibrium temperatures and masses, and have been singled out from the general population of close-in giant exoplanets for their high reflectances. A critical aspect of 51 Peg b is that, unlike *Kepler*-7b, it orbits a very bright star, and this entails an obvious advantage in achieving the required S/N. The fundamental assumptions adopted in the photometric model of our fiducial planet are easy to rescale for other planet–star configurations. Thus, the conclusions drawn from the exercise go beyond the specific case represented here. Other simplifications in our idealized analysis include: we ignore the impact of telluric absorption, sky brightness corrections, cross-talk between circular and linear polarizations, and the specifics of the detector performance (e.g., duty cycle, read-out noise). Telluric absorption may become problematic in the near-infrared, which is significantly affected by molecular oxygen and water bands. This may pose an additional challenge for the application of the technique to planets orbiting cool stars with rich spectra at these wavelengths. If the sky brightness originates from scattered moonlight, then its spectrum and Doppler shift are well known and can be removed (Donati et al. 2016). Cross-talk at the instrument level may produce spurious linear polarization (Bagnulo et al. 2009). If the lines in the spectrum of spurious linear polarization match the position of the lines in the stellar intensity spectrum, the distinct Doppler shift of the planet’s signal should facilitate the separation of each contribution. Figure 3 introduces some of the concepts in the photometric model.

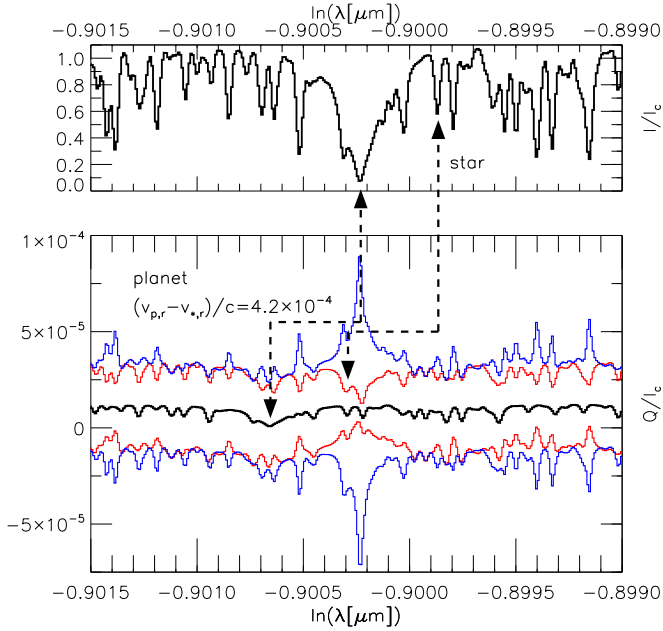


Figure 3. Top: continuum-normalized stellar intensity spectrum. Bottom: after occultation, for a phase angle $\alpha = -72^\circ$, the planet moves toward the observer with a velocity of $\approx 126 \text{ km s}^{-1}$, which causes a blueshift in the planet-reflected spectrum. Black: $(R_p/a)^2 Q' \mathcal{F}_*(\lambda - \lambda_D) / \mathcal{F}_{c,*}(\lambda)$ with $Q' = 0.05$, which produces a contrast of ~ 11 ppm in the continuum. Red: planet polarization plus/minus $\sigma_{\text{pn}}(\epsilon_I(\lambda)) / \mathcal{F}_{c,*}(\lambda)$. Blue: planet polarization plus/minus $\sigma_{\text{pn}}(\epsilon_I(\lambda)) / \mathcal{F}_{c,*}(\lambda) \times 1/T(\lambda)$. In both noise budget configurations ($b = 0$ and 1), the noise dominates over the planet polarization. The cross-correlation function exploits the redundancy of having multiple stellar lines over the measured spectrum to reduce the noise below the planet's signal. In the $b = 1$ configuration, the noise at the position of strong stellar absorption bands is significantly enlarged. The dashed arrows connecting the top and bottom graphs indicate the Doppler shift of the planet.

We adopted $a = 0.052 \text{ au}$, $V\text{-mag} = 5.5$, $M_p/M_J = 0.461$, $M_*/M_\odot = 1.054$, and $R_*/R_\odot = 1.025$ (as for the 51 Peg system³), and $R_p/R_J = 1.61$ (as for Kepler-7b) (Demory et al. 2011). For the stellar spectrum, we implemented Kurucz's very high-resolution solar spectrum,⁴ and corrected the solar irradiance \mathcal{F}_\odot to $\mathcal{F}_* = \mathcal{F}_\odot (\text{au}/d_*)^2$ with $d_* = 13.6 \text{ pc}$ so that $d_*/\text{au} = 2.512^{(V\text{-mag} + 26.74)/2}$. Without loss of generality, we also assumed that our fiducial planet is on a circular, edge-on (inclination $i = 90^\circ$) orbit that traces a straight line on the sky. Most transiting exoplanets are found in similar orbits and go through almost the full range of phase angles α from -180° to $+180^\circ$ as viewed from Earth. Although 51 Peg b is not occulted by its host star, we will refer to superior conjunction as the occultation phase. For a given orbital period, an $i = 90^\circ$ orbit maximizes the radial velocities of planet and star. Detecting the planet's radial velocity (whether in the intensity or polarization spectra) provides a determination of i with which to break the $M_p \sin(i)$ degeneracy from star-only radial velocities and in turn determine the true mass of the planet.

We define the reference plane for polarization to be perpendicular to the scattering plane. For $i = 90^\circ$, the reference plane projects on the sky as a straight line at a right angle to the planet's orbit. Q is the linear polarization component in the direction parallel ($Q > 0$) or perpendicular ($Q < 0$) to the reference plane, and U is the corresponding component at $\chi = \pm 45^\circ$. For a planet whose hemispheres north and south of

the scattering plane are not too different, the emergent linear polarization at $\chi = \pm 45^\circ$ will be minor and generally $|U'| \ll |Q'|$. Finding the direction at which U' vanishes provides a way to infer the orientation of the planet's orbit, a determination that is not possible with intensity-only measurements. That possibility comes at the cost of requiring, at least during an initial exploration, measurements in two directions rotated by 45° (or four to remove to first approximation the effect of instrumental polarization (Bagnulo et al. 2009)). For simplicity, we will assume in our calculations that the orientation of the planet's orbit on the sky is known and that the corresponding Stokes element Q is directly measurable with a single exposure and without additional rotations. The estimated exposure times can be properly rescaled if needed to relax these assumptions.

With the reference plane defined, the intensity and linear polarization observables of the planet–star system are represented in the photometric model through the expressions

$$m_I(\lambda; \alpha) = \left(\frac{R_p}{a}\right)^2 A_g(\lambda) \Phi(\lambda; \alpha) \mathcal{F}_*(\lambda - \delta\lambda_D) + \mathcal{F}_*(\lambda) + \epsilon_I(\lambda). \quad (1)$$

$$m_Q(\lambda; \alpha) = \left(\frac{R_p}{a}\right)^2 Q'(\lambda; \alpha) \mathcal{F}_*(\lambda - \delta\lambda_D) + m_Q^{\text{ISM}}(\lambda) + \epsilon_Q(\lambda). \quad (2)$$

We omit the corresponding m_U because if $|U'| \ll |Q'|$ it provides no information about the planet. We also omit the m_V term corresponding to circular polarization because cancellation between the northern and southern hemispheres is expected to make its value small (e.g., García Muñoz 2015; Wiktorowicz & Stam 2015). Both m_I and m_Q depend on wavelength λ and on the star–planet–observer phase angle α . Here, λ is defined on the rest reference frame of the star, and $\delta\lambda_D$ is the relative Doppler shift of the planet, i.e., $\delta\lambda_D/\lambda = (v_{*,r} - v_{p,r})/c$, where $v_{p,r} - v_{*,r}$ is the planet–star relative radial velocity (>0 if toward the observer) and c the speed of light. Typically, m_I will be dominated by the stellar flux $\mathcal{F}_*(\lambda)$. In our photometric model, $\epsilon_I(\lambda)$ represents both stellar photon noise and uncorrected systematics, and satisfies $\epsilon_I(\lambda) \ll \mathcal{F}_*(\lambda)$. The planet's contribution to m_I is scaled by $\mathcal{F}_*(\lambda - \delta\lambda_D)$, and considers the Doppler shift in the starlight spectrum reflected by the planet. It is tacitly assumed that the planet is tidally locked and that the lines in the measured stellar spectrum and in the planet-reflected spectrum are comparably broad.

In the observable m_Q of Equation (2), Q' contains the information on how the planet's atmosphere polarizes the incident starlight. Q' will generally vary with both wavelength and phase angle in ways that are unpredictable without detailed knowledge of the atmosphere (see Figure 1). $\epsilon_Q(\lambda)$ is analogous to $\epsilon_I(\lambda)$, and we adopt for their photon noise the standard deviations $\sigma_{\text{pn}}(\epsilon_Q(\lambda)) = \sigma_{\text{pn}}(\epsilon_I(\lambda)) = (\mathcal{F}_*(\lambda))^{1/2}$. We will further assume that $\epsilon_Q(\lambda)$ (and $\epsilon_I(\lambda)$, although the latter is not discussed) deteriorates with increasing photon noise at wavelengths near the core of strong stellar lines. Accordingly, we will describe $\epsilon_Q(\lambda)$ by means of a Gaussian random distribution with standard deviation $\sigma_{\text{pn}+\text{sys}}(\epsilon_Q(\lambda)) = \sigma_{\text{pn}}(\epsilon_Q(\lambda)) \times 1/T^b(\lambda)$. $\mathcal{T}(\lambda) = \mathcal{F}_*(\lambda)/\mathcal{F}_{c,*}(\lambda)$ is the continuum-normalized stellar spectrum, and $\mathcal{F}_{c,*}(\lambda)$ a low-order

³ <http://exoplanets.org>

⁴ <http://kurucz.harvard.edu/Sun/irradiance2005/irradthuwl.dat>

polynomial representation of the stellar continuum. $\mathcal{T}(\lambda)$ becomes small at the core of stellar lines and nearly one in the continuum. With $b > 0$ we adjust the potential impact of, e.g., an imperfect wavelength solution in the extraction of m_Q but also of other effects such as cross-talk in the instrument that are not explicitly represented in the photometric model. We refer to these effects as systematics, even though the term may not be fully representative of its intended meaning. b ranges from $b = 0$ (no impact, only photon noise) to $b \sim 1$ (major impact, systematics dominate the error budget at wavelengths matching strong stellar lines).

Three additional processes unrelated to the planet also contribute to m_Q . The first of them refers to the intrinsic polarization of the star, which occurs at the continuum and band level. For the Sun, the so-called second solar spectrum differs from the corresponding intensity spectrum, a fact that presents opportunities to investigate the solar atmosphere (Stenflo & Keller 1997). Upper limits on the broadband whole-disk fractional polarization of the Sun are 8×10^{-7} and 2×10^{-7} in B and V bands, respectively (Kemp et al. 1987). Such polarizations are likely smaller than the polarizations of close-in giant planets unless their atmospheres are very depolarizing. The second effect refers to the polarization of starlight by aligned, non-spherical dust grains in the ISM. Its broadband impact on the light reaching the telescope as a function of wavelength is often described in terms of the Serkowski law (Serkowski et al. 1973):

$$\frac{p^{\text{ISM}}(\lambda)}{p^{\text{ISM}}(\lambda_{\text{max}})} \approx \exp \left[-1.15 \ln^2 \left(\frac{\lambda_{\text{max}}}{\lambda} \right) \right]. \quad (3)$$

Here, $p^{\text{ISM}}(\lambda_{\text{max}})$ stands for the maximum fractional polarization, which occurs at λ_{max} . $p^{\text{ISM}}(\lambda)$ depends on the direction toward the star and its distance from Earth. Within the solar vicinity, this variation is typically ≤ 2 ppm pc^{-1} (Marshall et al. 2016), which may nevertheless suffice to dominate over the planet’s contribution. In our photometric model we will adopt $m_Q^{\text{ISM}}(\lambda) = p^{\text{ISM}}(\lambda) \mathcal{F}_*(\lambda)$ and $p^{\text{ISM}}(\lambda_{\text{max}} = 0.55 \mu\text{m}) = 30$ ppm. A key point in this simple description of $m_Q^{\text{ISM}}(\lambda)$ is that, if $p^{\text{ISM}}(\lambda)$ is a smooth function of wavelength as described by Equation (3), its contribution will peak in the CC function (CCF) at the velocity of the star. In that case, it might be possible to separate it from the planet polarization thanks to their relative Doppler shift, as discussed below. The third effect, physically related to the previous one, is the polarization of starlight introduced by the terrestrial atmosphere. In conditions of elevated dust content overhead at the observation site, the grains suspended in the atmosphere also polarize the incident starlight to levels of up to tens of ppm (Bailey et al. 2008). If uncorrected for, this telluric polarization will also bury the planet’s signal. In our photometric model, we will assimilate this latter effect into $m_Q^{\text{ISM}}(\lambda)$, thereby assuming that its wavelength dependence is also smooth.

For our fiducial planet, $(R_p/a)^2 \sim 220$ ppm, and if $Q' \sim 0.01$ – 0.05 , the fractional polarizations attributable to the planet in Equation (2), $Q' \times (R_p/a)^2$, are in the range 2 – 11 ppm. Such minute signals require between 7.4×10^{10} and 2.2×10^{12} photons to reduce the standard deviation of the stellar photon noise to $1/3$ of the signal. This estimate exposes one of the pitfalls of exoplanet polarimetry: that it is more photon-starved than photometry because Q' can be significantly

less than $A_g \Phi(\alpha)$. For reference, past broadband measurements for HD 189733 b have claimed upper limits on the planet polarization of ~ 30 – 60 ppm (Wiktorowicz et al. 2015; Bott et al. 2016).

For m_I and m_Q to represent observables at the telescope, they must incorporate a description of the optical system and the exposure time of the observations. If η stands for the end-to-end throughput of the entire optical system, D the primary mirror diameter of the telescope, and t_{expo} the integration time, the number of counts at the detector per spectral bin and the corresponding photon noise are obtained by replacing $\mathcal{F}_* \rightarrow \mathcal{F}_* \eta \pi (D/2)^2 t_{\text{expo}}$ in Equations (1) and (2). After this, the units of m_I and m_Q are counts per spectral bin. For our reference calculations, we adopt $\eta = 0.1$ and $D = 10$ m, and explore the impact of t_{expo} on the S/N. The numerical choice of η is motivated by the performance of existing high-dispersion spectro-polarimeters. Our nominal spectral grid adopts a resolving power $R = 60,000$ and assumes that each resolution element is sampled by two spectral bins. The grid is evenly spaced in $x = \ln \lambda$, and when covering the range 0.4 – $1 \mu\text{m}$ it comprises a total of $N = 2R \ln(1.0/0.4) \approx 110,000$ bins, each with $\Delta x = \Delta \lambda_i / \lambda_i = 1/2R \approx 8.3 \times 10^{-6}$. At maximum elongation, the relative planet–star radial velocity $v_p - v_* \approx v_p \approx 134 \text{ km s}^{-1}$ introduces a Doppler shift in the planet-reflected spectrum $\delta \lambda_D / \lambda \sim 4.5 \times 10^{-4}$, or up to 55 spectral bins for $R = 60,000$.

4. The CC function. Numerical Simulations

Sparks & Ford (2002) have described the fundamentals of the HDS-CC technique for the detection and atmospheric characterization of exoplanets. Many of the principles introduced in that work are directly applicable here, and we generally follow their treatment. Focusing on polarization, we set out to extract $(R_p/a)^2 Q'$ from m_Q (Equation (2)), the latter being the quantity determined at the telescope. For cross-correlation purposes, it is convenient to remove the low-frequency variations with wavelength in m_Q by introducing $\mu_Q = m_Q / \mathcal{F}_{c,*}$. Q' (and therefore μ_Q) is modulated in both wavelength and phase angle in a way that depends on the properties of the planet’s atmosphere being investigated. For the science cases of Figure 1, Q' at a phase angle $\alpha = -72^\circ$ varies by factors of up to ~ 6 when going from a wavelength of 0.4 to $1 \mu\text{m}$.

The success of the CC relies on proposing an accurate template for the planet’s signal hidden in the noise. Equation (2) shows that the planet polarization term is essentially a scaled-down, Doppler-shifted version of the stellar intensity spectrum, possibly modulated in wavelength by Q' . The continuum-normalized spectrum of the star $\mathcal{T}(\lambda)$ is thus an appropriate template to extract the contribution of the planet polarization from m_Q . In discretized form, we have $\mathcal{T}_i = \mathcal{T}(\lambda_i)$, with index i running over the N bins in the spectral grid. We also define $\hat{t}_i = \mathcal{T}_i / \sum \mathcal{T}_i - 1/N$ and $t'_i = N \mathcal{T}_i / \sum \mathcal{T}_i$, which satisfy $\langle \hat{t} \rangle = \sum \hat{t}_i / N \equiv 0$ and $\langle t' \rangle = \sum t'_i / N \equiv 1$ (Sparks & Ford 2002). The standard deviation of t' over a specified wavelength range, $\sigma(t')$, is a measure of how much structure exists in the template. In the current context, structure is equivalent to the spectrum having numerous strong lines. A small number of lines, or lines that are shallow, is equivalent to a spectrum without much structure. The concept is important because the more structured the template is, the less likely it is that a peak is

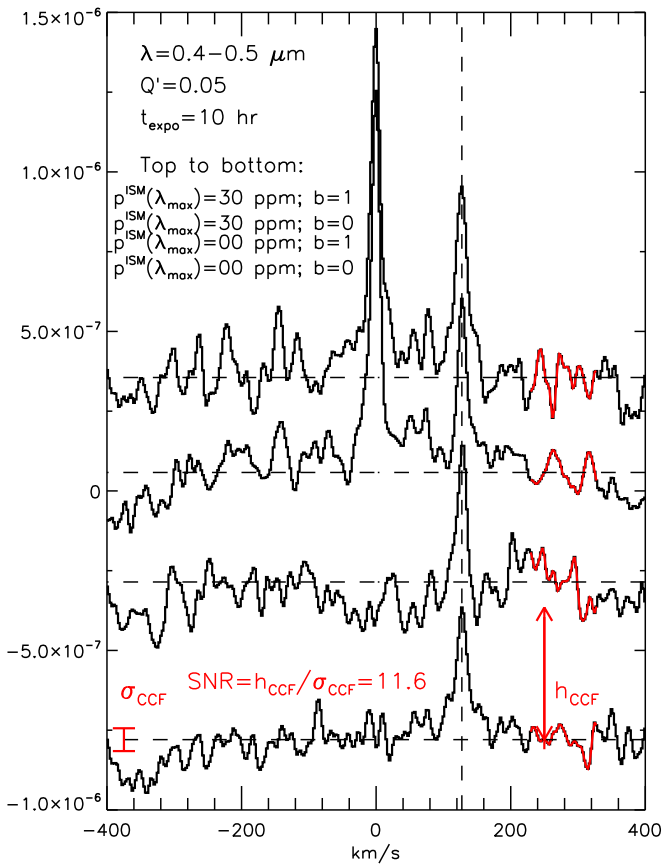


Figure 4. Examples of cross-correlation based on Equation (4) for the indicated configurations. The S/N is defined as the ratio of the CC peak height (subtracting the pedestal value estimated far from the peak) (right arrow, lowermost graph) over the standard deviation of the CC in the same continuum (red bar, lowermost graph). To estimate the continuum, we take a region between +100 and +200 km s⁻¹ from the planet (shown in red in the CC representation).

produced in the CCF by random noise because this should cancel out in the process of adding up the contributions from many spectral bins. Sparks & Ford (2002) provide theoretical arguments showing that the S/N achievable from the CC is indeed proportional to (and thus partly limited by) $\sigma(t')$. In practice, this means that the photons received over spectral regions with little structure (small $\sigma(t')$) are essentially useless to the effects of the CC. $\sigma(t')$ is straightforward to quantify from the stellar intensity spectrum; leaving aside considerations on the planet polarization, it provides a priori insight into which spectral regions are better behaved for application of the CC. We have done this for the Sun and obtained $\sigma(t') = 0.24, 0.14, 0.072, 0.052, 0.068$, and 0.041 for wavelengths in the ranges (in μm) $0.4\text{--}0.5$, $0.5\text{--}0.6$, $0.6\text{--}0.7$, $0.7\text{--}0.8$, $0.8\text{--}0.9$, and $0.9\text{--}1.0$, respectively. All other factors being equal, the calculated $\sigma(t')$ tells us that the HDSP-CC technique will use the stellar photons of solar-like stars a few times more efficiently at blue wavelengths than in the near-infrared. This disparate efficiency is dictated by the structure of the stellar spectrum, which is richer at the shorter wavelengths, and not by the integrated number of photons from each spectral interval, which is comparable in all cases.

In its simplest form, the CCF is formed by the operation

$$C_j = \sum_i \mu_{Q,i} \hat{t}_{i-j}. \quad (4)$$

For our nominal spectral grid, a shift by one bin is equivalent to a velocity displacement $v = (\Delta\lambda_i/\lambda_i)c \approx 2.5 \text{ km s}^{-1}$.

Figure 4 shows the CCF for $Q' = 0.05$, $t_{\text{expo}} = 10 \text{ hr}$, the spectral interval $0.4\text{--}0.5 \mu\text{m}$, and our reference telescope–instrument setup. Based on Figure 1, it is assumed that $\alpha = -72^\circ$, which sets the planet–star relative radial velocity to $\sim 127 \text{ km s}^{-1}$. The four CCFs explore four combinations of the prescribed m_Q^{ISM} ($p^{\text{ISM}}(\lambda_{\text{max}} = 0.55 \mu\text{m}) = 0$ and 30 ppm ; Equation (3)) and the contribution of systematics to the overall noise budget ($b = 0$ and 1). The S/N is defined by the ratio of the peak-to-wing height of the CCF and the standard deviation in a region of the CCF far enough from the peak, i.e., $S/N = h_{\text{CCF}}/\sigma_{\text{CCF}}$. The S/Ns estimated in Figure 4 are comparable and in the range 7–13. The specific S/N for any one example is partly dictated by random noise and varies between simulations. A main conclusion from Figure 4 is that the planet peak in the CCF is well separated from the stellar peak (centered at zero velocity), and that it is possible to unambiguously detect the planet’s signal with hours of exposure time, depending on Q' and the other assumed properties of the photometric model. We have not conducted an assessment of false-alarm probabilities, but a visual inspection over numerous simulations suggests that a robust detection of the planet peak requires $S/N \geq 5\text{--}6$.

We have estimated the S/N for other configurations relevant to the science case introduced in Section 2. Based on the above, we safely adopted $p^{\text{ISM}}(\lambda_{\text{max}} = 0.55 \mu\text{m}) = 0$ and $b = 0$. Motivated by the phase curves in Figure 1, we again considered an orbital position with $\alpha = -72^\circ$ and three possible behaviors for $Q'(\lambda)$. $Q'(\lambda) = 0.01$ is a pessimistic scenario with a weak planet polarization of $(R_p/a)^2 Q' \sim 2 \text{ ppm}$. $Q'(\lambda) = 0.05$, and independent of wavelength, is a plausible representation for an atmosphere with a top layer that is moderately polarizing (Figure 1(top), triangles), and results in $(R_p/a)^2 Q' \sim 11 \text{ ppm}$. Finally, we considered a $Q'(\lambda)$ that varies with wavelength as in the silicate cloud case of Figures 1(top-bottom). In this case, the planet polarizes weakly ($Q' < 0.01$) in the blue but moderately ($Q' > 0.06$) in the near-infrared, which also means that Q' and $\sigma(t')$ (for the solar spectrum) vary in the reverse orders with wavelength. The $Q'(\lambda)$ behavior for this latter case is shown in Figure 5(a).

The results of the S/N analysis are summarized in Figures 5(b)–(e) for the reference telescope–instrument setup ($\eta = 0.1$, $D = 10 \text{ m}$, $R = 60,000$). Black, red, and magenta colors are specific to the $Q' = 0.01$, $Q' = 0.05$, and silicate scenarios described above, respectively. The graphs refer to exposure times increasing from top to bottom. According to our photometric model, an exposure of 160 hr at a 10 m telescope is equivalent to a 10 hr exposure from a future 40 m class telescope. The width of the horizontal bars in the S/N representations conveys the assumed wavelength range for the observations.

At least four factors must be considered when proposing a wavelength range for observations. The first one is that in general a narrow interval (say, $0.1 \mu\text{m}$) will ensure that Q' is nearly constant over it and therefore \hat{t} remains a better template for the planet polarization term in μ_Q . The second one is that extending the observations to wavelengths at which Q' is small may hamper rather than help the detection. The third one is that a larger interval means that more photons are collected overall, although this does not necessarily translate into a better S/N. Finally, the fourth factor refers to the level of structure in the

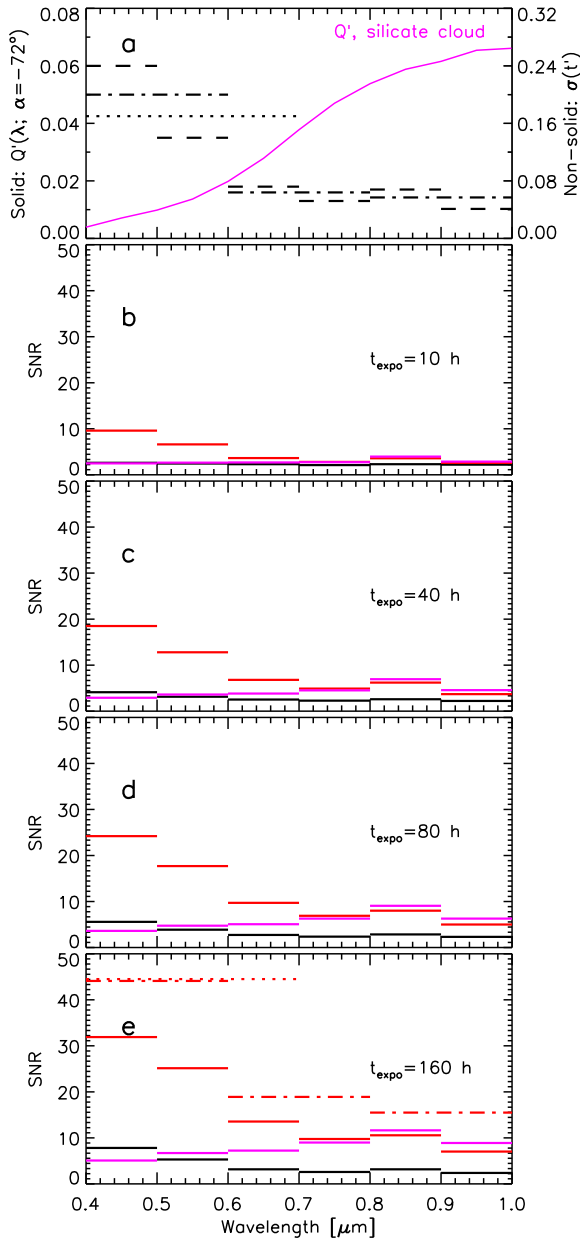


Figure 5. (a) Solid: polarization element Q' as a function of wavelength in the post-occultation configuration $\alpha = -72^\circ$ for silicate cloud particles (Figure 1). The planet polarizes more efficiently at the longer wavelengths. The cases $Q' = 0.01$ and 0.05 , independent of wavelength, are specifically developed in graphs (b)–(e) with black and red colors, respectively. Non-solid: standard deviation of the normalized form of the stellar spectrum t' over the indicated wavelengths. The stellar spectrum is significantly more structured at the shorter wavelengths. Considering wavelength ranges of different size (from 0.1 up to $0.3 \mu\text{m}$) reveals that a larger spectral coverage does not necessarily result in better S/Ns. The magnitude of Q' and its wavelength dependence, the total number of collected photons and the structure of the stellar spectrum over the specified wavelength range, as quantified by $\sigma(t')$, can partly compensate (see text). (b)–(e) S/N calculated as described in the text for $Q' = 0.01$ (black), $Q' = 0.05$ (red), and the wavelength-dependent Q' described in the top graph for silicate cloud particles. Each graph refers to an exposure time from 10 to 160 hr in our reference scenario. We adopted for the S/N calculations $p^{\text{ISM}}(\lambda_{\text{max}} = 0.55 \mu\text{m}) = 0$ and $b = 0$ (Figure 4). The quoted S/Ns are median values based on a few hundred random realizations of the noise terms in m_Q (Equation (2)).

template, as quantified by $\sigma(t')$, over the specific spectral region. If the spectral region shows little structure (small $\sigma(t')$), it will help little (or nothing) toward detecting the planet

polarization. Some of these factors are potentially in mutual conflict. And for those depending on the magnitude and shape of Q' there is limited a priori information that can be used to optimize the selection of wavelengths. Obviously, if the observations are made over a broad wavelength range, there is always the option of forming smaller spectral ranges in the post-observation analysis. The cases investigated in Figure 5 demonstrate some of these possibilities by considering a variety of wavelength ranges over the spectrum. They are (in μm): $0.4\text{--}0.5$, $0.5\text{--}0.6$, $0.7\text{--}0.8$, $0.8\text{--}0.9$, $0.9\text{--}1$ (dashed); $0.4\text{--}0.6$, $0.6\text{--}0.8$, $0.8\text{--}1$ (dashed-dotted); $0.4\text{--}0.7$ (dotted).

The case with $Q' = 0.01$ (black bars) is always difficult to detect above our tentative detection threshold of $S/N = 6$. A convincing detection is possible though for the longest exposure time ($t_{\text{expo}} = 160$ hr) and shortest wavelengths ($0.4\text{--}0.5$ and $0.5\text{--}0.6 \mu\text{m}$). Unsurprisingly, the configuration with $Q' = 0.05$ (red bars) is much less challenging, and would be detectable with less than $t_{\text{expo}} = 10$ hr at short wavelengths. At the longer wavelengths, however, the drop in $\sigma(t')$ implies that much longer integration times are needed. The dependence of the S/N on $\sigma(t')$ is clearly seen in the configuration with $Q' = 0.05$ and $t_{\text{expo}} = 160$ hr (bottom graph, red bars, and compare with top graph, black bars). In this case, the S/N scales almost exactly with $\sigma(t')$ and makes the S/N at short wavelengths larger by a factor of a few than in the near-infrared. The bottom graph reveals also the effect of enlarging the wavelength interval. The improvement in S/N when integrating over $0.4\text{--}0.6 \mu\text{m}$ with respect to the corresponding S/Ns at $0.4\text{--}0.5$ or $0.5\text{--}0.6 \mu\text{m}$ is mainly driven by the increased number of photons in the larger interval. However, extending the wavelength interval to $0.4\text{--}0.7 \mu\text{m}$ is compensated for by decreasing $\sigma(t')$ values and does not result in an improved overall S/N. The simulations with $Q' = 0.01$ and 0.05 show also that the estimated S/N increases as the magnitude of Q' or the exposure time increases, but in a manner slower than linear.

Finally, the case of Q' consistent with the silicate cloud (magenta) shows the compensating effects of a template that becomes less structured toward the long wavelengths while the planet polarization signal becomes stronger. The simulations show that the resulting S/N peaks at wavelengths from 0.8 to $0.9 \mu\text{m}$, and that this could be detected in ~ 40 hr of integration time. The confirmation of the silicate cloud configuration at all wavelengths from 0.4 to $1 \mu\text{m}$ would take ~ 160 hr at each spectral range of $0.1 \mu\text{m}$.

Finally, a few words on the efficiency with which the HDSP-CC technique utilizes the collected light. We integrated the first term on the right of Equation (2) over the spectral direction to calculate the number of counts at the detector originating from planet polarization, and called this amount $s_{p,Q}$. We similarly added up the counts arriving directly from the star, and called that S_* . $(S/N)_{\text{lim}} = s_{p,Q}/\sqrt{S_*}$ is the limiting S/N that might be achieved if stellar photon noise dominates the noise budget. The comparison of the CCF-based S/N and $(S/N)_{\text{lim}}$ reveals that $(S/N)/(S/N)_{\text{lim}} \sim \sigma(t')$ (Sparks & Ford 2002). The reason for this reduced efficiency of the HDSP-CC technique versus broadband polarimetry is that the HDSP-CC technique benefits only from photons in spectral regions that are highly structured. The photons collected in regions with little structure are essentially useless. Unlike broadband polarimetry, however, the HDSP-CC offers an intrinsic way to discriminate between polarization arising at the planet and other sources of polarization provided that the different polarization sources are Doppler-shifted. Finally, we have explored the S/Ns estimated

in Figure 5 at resolving powers as low as $R = 10,000$, and found that on average the corresponding S/Ns are reduced by less than 20%–30%. Thus, somewhat lower resolving powers do not significantly affect the power of the HDSP-CC technique.

5. Discussion and Summary

We have discussed the HDSP-CC technique and its application to the investigation of exoplanet polarization. The effort is motivated by the potential of polarimetry to offer insight into exoplanet atmospheres that is not possible with other techniques, and by the present and near-future availability of telescopes and instruments with which to carry out such observations. We presented plausible multi-wavelength polarization simulations of the close-in giant exoplanet Kepler-7b, for which broadband, optical brightness phase curves have already provided partial characterization of its atmosphere. Assuming that the atmospheric properties of the non-transiting, bright-host hot Jupiter 51 Peg b are not too different from those simulated for Kepler-7b, we show that the polarization of 51 Peg b might be an accessible target for a dedicated observational effort. Larger collecting areas will bring the possibility of targeting fainter host stars and smaller planets, and therefore the proposed technique may develop its full potential with the advent of 30–40 m class telescopes in the next decade. The characterization of exoplanet atmospheres with the HDSP-CC technique thus represents a valuable science case for the development of such instruments. Particularly interesting is the future possibility of targeting planets within their habitable zones to investigate through polarization their gas composition (Stam et al. 2004) or the occurrence of water clouds on them (Bailey 2007; García Muñoz 2015). A related instrument concept that may one day fly is *LUVOIR*/POLLUX, focused on the ultraviolet. Short wavelengths represent a gain in the structure of the stellar spectrum and therefore in the efficiency of the HDSP-CC technique, provided that the planet is sufficiently reflective and polarizing at such wavelengths. A detailed study will help to establish the relevant trade-offs in the design of observations of reflected starlight polarization at ultraviolet wavelengths.

In our idealized analysis, we did not address the inverse problem of inferring the planet polarization from simulated observations. Such an exercise will depend on the specifics of each facility, and might have to consider a range of $Q'(\lambda; \alpha)$ representations with the goal of maximizing a figure of merit (e.g., the CCF peak or the S/N).

In principle, the HDSP-CC technique can also be applied to the detection of atomic and molecular absorption in polarization spectra. Sparks & Ford (2002) and Lovis et al. (2017) have discussed some of the practicalities for the detection of absorption features in brightness spectra. A possible strategy involves the construction of templates that contain the contribution from various amounts of the gas whose existence is suspected. In terms of the photometric model, this means that the term $Q'(\lambda; \alpha)$ in Equation (2) incorporates the continuum reflection by the gas (Rayleigh scattering) and cloud particles (as done here), together with the effect of narrowband absorption by atoms and molecules (not done here). The template spectrum that optimizes the CCF on the basis of a selected figure of merit would point to the most plausible atmospheric configuration. Molecules with complex spectra at high resolution will likely provide the required structure to make the molecule stand out in the CCF (Rodler &

López-Morales 2014). For close-in giant exoplanets such as 51 Peg b, H₂O and TiO may be plausible targets for such searches (Sing et al. 2016; Sedaghati et al. 2017). Further into the future, the search for molecular absorption might also target gases associated with potential habitability conditions on the planet (e.g., O₂, H₂O, or CH₄), all of which absorb at visible–NIR wavelengths. Indeed, the simulations by Stam (2008) and Emde et al. (2017) for various Earth-like atmospheric configurations show that some of these molecules introduce significant structure in the Q spectrum of polarized intensity. Whether it is more convenient to detect the molecules in the brightness spectrum or in the polarization spectrum will depend partly on the depth of the absorption lines in the corresponding spectra and on the total number of photons that can be collected in each case. It will also be interesting to find out what additional information could be inferred from the simultaneous detection of a molecule in both the brightness and polarization spectra.

Finally, Lovis et al. (2017) have shown that a 10 m telescope with the combined capability to partly reject the stellar glare at the planet’s location through a high-contrast imager and to disperse the collected light at high spectral resolution can constrain the albedo of Proxima Centauri b (Anglada-Escudé et al. 2016) and detect the possible occurrence of O₂, H₂O, or CH₄ in its reflected brightness spectrum in about 60 nights of telescope time. Provided that the planet polarizes efficiently, as expected for some Earth-like atmospheric configurations (Stam 2008; García Muñoz 2015; Emde et al. 2017), and that a similarly efficient form of high-contrast imager can be utilized simultaneously, it might be conceivable to detect Proxima Centauri b’s polarization either in the continuum or in molecular absorption bands. Since the number of polarized photons observed is less than the total number of photons, the effort of such a search is expected to be larger than, but overall of the same order as, for a search in brightness.

The following summarizes some of the other points discussed earlier.

1. Polarimetry is a valuable complement to photometric and spectroscopic measurements in the atmospheric characterization and mapping of exoplanets.
2. The HDSP-CC technique offers a built-in way to separate polarization contributions originating with different radial velocities. This may prove useful for disentangling the planet polarization from the polarization introduced by the ISM and the terrestrial atmosphere. It may also prove useful for removing the effect of systematics provided that the systematics signal is either a smooth function of wavelength or mimics the stellar spectrum without shifts in wavelength.
3. The optimal choice of wavelength for application of the HDSP-CC technique will depend on properties of both the planet and the star.
4. Predicting the polarization properties of an exoplanet atmosphere is challenging. Even when other techniques (e.g., transmission spectroscopy, brightness phase curves) have shed some light on the atmospheric structure, the emergent polarization will be sensitive to weakly constrained properties such as the composition and size of condensates within about one optical depth from the top of the atmosphere. Inversely, polarization measurements will set valuable constraints on such properties.
5. The HDSP-CC technique is less efficient than broadband polarimetry in its use of collected photons. The light collected over wavelengths at which the stellar spectrum is

not strongly structured is essentially wasted. The expected efficiency can be quantified prior to the observations.

6. If Rayleigh scattering dominates the planet polarization, the best range of orbital phases to investigate the planet is closer to $\alpha \sim 60^\circ\text{--}80^\circ$ (where the polarization intensity Q' is maximum) than to 90° (where the planet fractional polarization $Q'/A_g\Phi(\alpha)$ is maximum).
7. The brightness phase curves of giant exoplanets often exhibit post-occultation brightness peaks attributed to non-uniform clouds. Our model simulations show that for such configurations Q' also peaks after occultation. If possible, the observations of such planets, also in polarization, should favor post-occultation phases.
8. The ideal observation targets exhibit large brightness and polarization magnitudes, although the two properties are not always compatible because they depend on the details of multiple scattering in the atmosphere. Brightness phase curves may guide the identification of potential targets to follow up with polarimetry. 51 Peg b remains a good candidate for both brightness and polarization measurements in the immediate future.
9. The planet polarization is very sensitive to both the phase angle and wavelength of the observations. Accumulating observations over a broad range of phase angles may wash out some of that dependence. Selecting the optimal phase angle to observe, however, is not trivial. A reasonable (although not failure-proof) approach may be to assume that Rayleigh scattering will be prominent, thereby favoring phase angles in the range $\alpha \sim 60^\circ\text{--}80^\circ$.

Ultimately, the simulations presented here encourage dedicated observations from current and future facilities equipped with high-dispersion spectro-polarimeters.

I thank Klaus Strassmeier and Ilya Ilyin (Leibniz-Institute for Astrophysics Potsdam, Germany) for encouragement and a useful exchange of information at an early stage of the project. Special thanks go to Luca Fossati (Space Research Institute, Austrian Academy of Sciences, Austria) for a thorough reading of the manuscript together with helpful and constructive comments.

ORCID iDs

A. García Muñoz  <https://orcid.org/0000-0003-1756-4825>

References

- Angerhausen, D., DeLarme, E., & Morse, J. A. 2015, *PASP*, **127**, 1113
- Anglada-Escudé, G., Amado, P. J., Barnes, J., et al. 2016, *Natur*, **536**, 437
- Artigau, É., Kouach, D., Donati, J.-F., et al. 2014, *Proc. SPIE*, **9147**, 914715
- Bagnulo, S., Landolfi, M., Landstreet, J. D., et al. 2009, *PASP*, **121**, 993
- Bailey, J. 2007, *AsBio*, **7**, 320
- Bailey, J., Kedziora-Chudczer, L., Cotton, D. V., et al. 2015, *MNRAS*, **449**, 3064
- Bailey, J., Ulanowski, Z., Lucas, P. W., et al. 2008, *MNRAS*, **386**, 1016
- Berdyugina, S. V., Berdyugin, A. V., Fluri, D. M., & Piirola, V. 2008, *ApJL*, **673**, L83
- Berdyugina, S. V., Berdyugin, A. V., Fluri, D. M., & Piirola, V. 2011, *ApJL*, **728**, L6
- Bott, K., Bailey, J., Kedziora-Chudczer, L., et al. 2016, *MNRAS*, **459**, L109
- Buenzli, E., & Schmid, H. M. 2009, *A&A*, **504**, 259
- Charbonneau, D., Noyes, R. W., Korzennik, S. G., Nisenson, P., & Jha, S. 1998, *ApJL*, **522**, L145
- Cikota, A., Patat, F., Cikota, S., & Faran, T. 2017, *MNRAS*, **464**, 4146
- Collier Cameron, A., Horne, K., Penny, A., & James, D. 1999, *Natur*, **402**, 751
- Cotton, D. V., Bailey, J., Kedziora-Chudczer, L., et al. 2016, *MNRAS*, **455**, 1607
- Cotton, D. V., Marshall, J. P., Bailey, J., et al. 2017, *MNRAS*, **467**, 873
- Demory, B.-O., de Wit, J., Lewis, N., et al. 2013, *ApJL*, **776**, L25
- Demory, B.-O., Seager, S., Madhusudhan, N., et al. 2011, *ApJL*, **735**, L12
- Donati, J.-F., Catala, C., Landstreet, J. D., & Petit, P. 2006, in ASP Conf. Ser. 358, *Solar Polarization 4*, ed. R. Cassini & B. W. Lites (San Francisco, CA: ASP), 362
- Donati, J.-F., Moutou, C., Malo, L., Baruteau, C., Yu, L., et al. 2016, *Natur*, **534**, 662
- Emde, C., Buras-Schnell, R., Sterzik, M., & Bagnulo, S. 2017, *A&A*, **605**, A2
- Esteves, L. J., De Mooij, E. J. W., & Jayawardhana, R. 2015, *ApJ*, **804**, 150
- Fluri, D. M., & Berdyugina, S. V. 2010, *A&A*, **512**, A59
- Fortier, A., Beck, T., Benz, W., et al. 2014, *Proc. SPIE*, **9143**, 91432J
- Fossati, L., Bagnulo, S., Haswell, C. A., et al. 2012, *ApJL*, **757**, L15
- Fossati, L., Bagnulo, S., Mason, E., & Landi Degl'Innocenti, E. 2007, in ASP Conf. Ser., 364, *The Future of Photometric, Spectrophotometric and Polarimetric Standardization*, ed. C. Sterken (San Francisco, CA: ASP), 503
- García Muñoz, A. 2015, *IJAsB*, **14**, 379
- García Muñoz, A., & Isaak, K. G. 2015, *PNAS*, **112**, 13461
- García Muñoz, A., & Mills, F. P. 2015, *A&A*, **573**, A72
- Hansen, J. E., & Hovenier, J. W. 1974, *JATIS*, **31**, 1137
- Hansen, J. E., & Travis, L. D. 1974, *SSRv*, **16**, 527
- Hu, R., Demory, B.-O., Seager, S., Lewis, N., & Showman, A. 2015, *ApJ*, **802**, 51
- Kemp, J. C., Henson, G. D., Steiner, C. T., & Powell, E. R. 1987, *Natur*, **326**, 270
- Kolokolova, L., Hough, J., & Levasseur-Regourd, A.-Ch. 2015, *Polarimetry of Stars and Planetary Systems* (Cambridge: Cambridge Univ. Press)
- Latham, D. W., Borucki, W. J., Koch, D. G., et al. 2010, *ApJL*, **713**, L140
- Lavvas, P., Yelle, R. V., Koskinen, T., et al. 2013, *PNAS*, **110**, 2729
- Lecavelier des Etangs, A., Vidal-Madjar, A., Désert, J.-M., & Sing, D. 2008, *A&A*, **485**, 865
- Lovis, C., Snellen, I., Mouillet, D., Pepe, F., Wildi, F., et al. 2017, *A&A*, **599**, A16
- Lucas, P. W., Hough, J. H., Bailey, J. A., et al. 2009, *MNRAS*, **393**, 229
- Marshall, J. P., Cotton, D. V., Bott, K., et al. 2016, *ApJ*, **825**, 124
- Martins, J. H. C., Santos, N. C., Figueira, P., et al. 2015, *A&A*, **576**, A134
- Mishchenko, M. I., Travis, L. D., & Lacis, A. A. 2002, *Scattering, Absorption, and Emission of Light by Small Particles* (Cambridge: Cambridge Univ. Press)
- Mishchenko, M. I., Rosenbush, V. K., Kiselev, N. N., et al. 2010, *Polarimetric Remote Sensing of Solar System Objects* (Kyiv: Akadempriodyka)
- Moutou, C., Donati, J.-F., Savalle, R., et al. 2007, *A&A*, **473**, 651
- Oreshenko, M., Heng, K., & Demory, B.-O. 2016, *MNRAS*, **457**, 3420
- Parmentier, V., Fortney, J. J., Showman, A. P., Morley, C., & Marley, M. S. 2016, *ApJ*, **828**, 22
- Rauer, H., Catala, C., Aerts, C., et al. 2014, *ExA*, **38**, 249
- Ricker, G. R., Winn, J. N., Vanderspek, R., et al. 2015, *JATIS*, **1**, 014003
- Rodler, F., Kürster, M., López-Morales, M., & Ribas, I. 2013, *AN*, **334**, 188
- Rodler, F., & López-Morales, M. 2014, *ApJ*, **781**, 54
- Rodler, F., López-Morales, M., & Ribas, I. 2012, *ApJL*, **753**, L25
- Roman, M., & Rauscher, E. 2017, *ApJ*, **850**, 17
- Seager, S., Whitney, B. A., & Sasselov, D. D. 2000, *ApJ*, **540**, 504
- Sedaghati, E., Boffin, H. M. J., MacDonald, R. J., et al. 2017, *Natur*, **549**, 238
- Serkowski, K. 1973, in IAU Symp. 52, *Interstellar Dust and Related Topics*, ed. J. M. Greenberg & H. C. Van de Hulst (Dordrecht: Reidel), 145
- Showman, A. P., Cooper, C. S., Fortney, J. J., & Marley, M. S. 2008, *ApJ*, **682**, 559
- Shporer, A. 2017, *PASP*, **129**, 072001
- Sing, D. K., Fortney, J. J., Nikolov, N., et al. 2016, *Natur*, **529**, 59
- Snellen, I. A. G., Brandl, B. R., de Kok, R. J., et al. 2014, *Natur*, **509**, 63
- Snellen, I. A. G., de Kok, R. J., de Mooij, E. J. W., & Albrecht, S. 2010, *Natur*, **465**, 1049
- Snik, F., Jeffers, S., Keller, C., et al. 2008, *Proc. SPIE*, **7014**, 70140
- Sparks, W. B., & Ford, H. C. 2002, *ApJ*, **578**, 543
- Stam, D. M. 2008, *A&A*, **482**, 989
- Stam, D. M., Hovenier, J. W., & Waters, L. B. F. M. 2004, *A&A*, **428**, 663
- Stenflo, J. O., & Keller, C. U. 1997, *A&A*, **321**, 927
- Strassmeier, K. G., Ilyin, I., Järvinen, A., et al. 2015, *AN*, **336**, 324
- Sudarsky, D., Burrows, A., & Pinto, P. 2000, *ApJ*, **538**, 885
- Tomasko, M. G., & Smith, P. H. 1982, *Icar*, **51**, 65
- West, R. A., Lane, A. L., Hart, H., et al. 1983, *JGR*, **88**, 8699
- West, R. A., & Smith, P. H. 1991, *Icar*, **90**, 330
- Wiktorowicz, S. J. 2009, *ApJ*, **696**, 1116
- Wiktorowicz, S. J., Nofi, L. A., Jontof-Hutter, D., et al. 2015, *ApJ*, **813**, 48
- Wiktorowicz, S. J., & Stam, D. M. 2015, in *Polarimetry of Stars and Planetary Systems*, ed. L. Kolokolova, J. Hough, & A.-C. Levasseur-Regourd (Cambridge: Cambridge Univ. Press), 439